An X-ray/H.E.S.S. study of the spatially resolved properties of the PWN MSH 15−52 using MHD principles

Fabian M. Schoeck*, Ingo Buesching†, Peter Eger*, Okkie C. de Jager†, Matthieu Renaud‡ and Michael Vorster†

*Erlangen Centre for Astroparticle Physics, Erwin-Rommel-Strasse 1, 91054 Erlangen, Germany
†Unit for Space Physics, North-West University, Potchefstroom, 2520, South Africa
‡APC, CNRS, Université Denis Diderot Paris 7, Paris, France

Abstract. **The pulsar wind nebula (PWN) MSH 15−52 shows well-resolved jet-like emission in X-rays and TeV γ-rays. It is powered by the energetic 150 ms pulsar PSR B1509−58 with an age of about $1,700$ yr and a spin-down luminosity of around 1.8×10^{37} erg/s. Given the pre-reverse shock evolutionary status of the PWN, this source serves as a very good candidate to test analytical models for the post-shocked PWN particle spectrum. By determining the spatially resolved spectral parameters in the X-ray domain using MHD principles, we should be able to provide constraints on the expected VHE gamma-ray spectrum of the jet-region, which we then compare with the measured emission as seen by the H.E.S.S. telescope system. Finally, with the aid of the well-resolved H.E.S.S. spectrum, we attempt to obtain a more restrictive constraint on the PWN shock parameters.**

***Keywords*: Pulsar Wind Nebulae, MHD Modeling, MSH 15−52**

I. Introduction

MSH 15−52 (G320.4−1.2) is a complex Supernova Remnant (SNR) which was discovered in radio wavelenghts in 1961 by Mills et al. [1]. Its radio appearance is dominated by two spots, a brighter one to the northwest and a fainter one to the southeast. The radio emission to the northwest coincides spatially with the H II region RCW 89. Inside the SNR lies the energetic 150 ms pulsar PSR B1509−58, discovered by the Einstein satellite [2]. It has a spin-down luminosity of $\dot{E} = 1.8 \times 10^{37}$ erg/s and a characteristic age $\tau = 1.7$ kyr [3]. This makes the pulsar one of the youngest and most energetic known. Gaensler et al. [4] concluded by a comparison of the radio and the X-ray emission that MSH 15−52, PSR B1509−58 and RCW 89 are associated objects and lie at a distance of 5.2 ± 1.4 kpc.

X-ray observations of the SNR showed the existence of a Pulsar Wind Nebula (PWN) powered by PSR B1509−58 ([5] and [6]). More detailed observations with the Chandra satellite revealed two outflow jets in the southeast and northwest direction, the latter being terminated in the optical nebula RCW 89 ([7]). For the diffuse PWN they derived a power-law photon index of 2.05 ± 0.04 and an absorbtion column density of $(9.5 \pm 0.3) \times 10^{21}$ cm^{-2}. The hard X-ray spectrum of the PWN was observed with the BeppoSAX and the INTEGRAL satellites, which observed emission described by a power-law with an index of 2.1 ([8] and [9]).

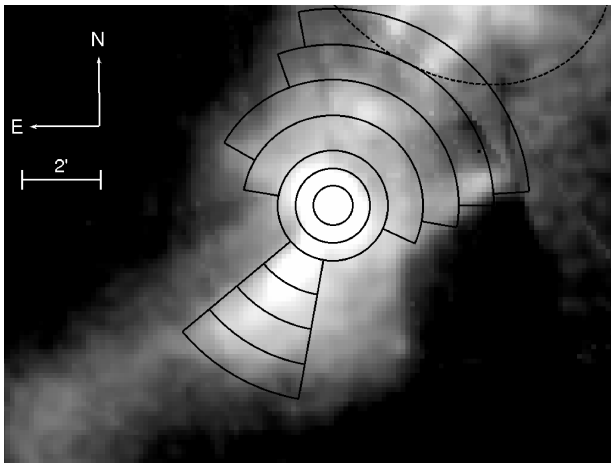

Fig. 1. XMM-Newton count map of MSH 15−52 showing the six extraction regions (solid lines) and the exclusion (dashed line) region used for the spectral analysis. The two inner regions are full rings, whereas the four outer regions consist of the addition of subrings to the NW and the SE.

In the very high energy (VHE; 100 GeV-100 TeV) γ-ray domain, the PWN was observed by the High Energy Stereoscopic System (H.E.S.S.). The source is clearly extended beyond the point spread function and shows a comparable morphology as in X-rays, extending to the northwest and southeast of the pulsar. The observed γ-ray emission is well-fitted by a power-law with a photon index of 2.27 up to a photon energy of 40 TeV [10].

Here we present the first analysis of the public XMM-Newton data of the PWN MSH 15−52 and a model based on the principles of magnetohydrodynamics (MHD) to describe the observed emission in the X-ray domain. We want to use the model parameters derived to make predictions for the VHE γ-ray emission as observed by the H.E.S.S. Cherenkov telescope array.

II. XMM-Newton observations

The region around the SNR MSH 15−52 has been observed six times with XMM-Newton [11] with the

TABLE I
DETAILS OF THE XMM-NEWTON EPIC PN OBSERVATIONS

Observation ID	Exposures (ks) performed[1]	net[2]
0207050201	23.135	5.9
0302730201	16.130	3.6
0302730301	8.235	2.0

[1] Exposure time without background screening
[2] Net exposure time after background screening

TABLE II
EXTRACTION REGIONS

Ring No.	Radius (") in	out	Angles[1] (°) SE	NW
1	30	57	full ring	
2	57	84	full ring	
3	84	138	220 - 260	335 - 170
4	138	192	220 - 260	350 - 150
5	192	246	220 - 260	0 - 110
6	246	300	220 - 260	4 - 100

[1] Angles measured counter-clockwise from west.

EPIC-MOS [12] and EPIC-PN [13] cameras. These pointings were either centered north or southeast of the pulsar PSR B1509−58. During one of those pointings (obsid: 0312590101), all three cameras were operated in timing mode. Therefore this observation will not be considered in this paper.

In order to study the morphology-dependent spectral characteristics of the extended emission, we require the whole area of our interest to be within the FoV. Only the three observations pointing towards the northern region matched this criterium (obsid: 0207050201, 0302730201 and 0302730301).

To analyze the X-ray data we used the XMM-Newton Science Analysis System (SAS) version 8.0.0 supported by tools from the FTOOLS package together with XSPEC version 12.5.0 for spectral modeling. To definine good time intervals (GTI) we applied a rather conservative background threshold of 10 background cts/s. In this work we only analyzed the data of the PN camera since it is the most sensitive instrument. All observations were affected by long periods of background flaring or full scientific buffer of the PN camera which led to rather short net exposures (see Tab. I). However, the statistics were still sufficient to extract spectra from all regions.

III. X-RAY SPECTRA

To study the radial dependence of the spectral properties of the extended emission of the PWN we extracted spectra from annular regions centered on the pulsar position (R.A.: 15:13:55, Dec.: -59:08:08.8). Due to the strong spatial inhomogeneity of the X-ray emission we did not extract events from the full rings but from wedge-shaped sectors along the southeast and northwest directions to increase the signal to background ratio (see Tab. II and Fig. 1).

In order to avoid systematic effects from CCD borders, we extracted the spectra for each detector CCD seperately and merged them afterwards by weighting the responses (rmf) and auxilliary responses (arf) with the size of the respective extraction region. The effective areas were calculated by weighting the contribution from each pixel with the flux using a detector map from the 0.2-7 keV energy band.

For each ring the spectra from the three observations were fit in parallel with an absorbed powerlaw model. The parameters for column density and photon index were linked, whereas the norm was free to vary between the spectra to account for changes in the extraction area caused by bad columns or different orientations of CCD borders in the observations.

TABLE III
RESULTS FROM SPECTRAL FITTING

Ring No.	N_H (10^{22} cm^{-2})	Γ	Flux (10^{-12} erg cm^{-2} s^{-1})
1	1.15 ± 0.03	1.66 ± 0.03	11.2 ± 0.4
2	1.14 ± 0.04	1.79 ± 0.04	$9.7^{+0.5}_{-0.2}$
3	1.22 ± 0.03	1.98 ± 0.03	16.2 ± 0.5
4	1.20 ± 0.03	2.04 ± 0.04	$17.0^{+0.5}_{-0.6}$
5	1.19 ± 0.04	2.07 ± 0.04	10.5 ± 0.4
6	1.15 ± 0.07	2.03 ± 0.07	$5.2^{+0.4}_{-0.3}$

The resulting parameters for each ring are listed in Table III. The absorption column densities N_H are in agreement between the different regions. The index Γ of the fitted absorbed powerlaw increases from the inner regions to the outer regions by roughly 0.5, reflecting a softening of the spectrum with increasing distance. Fig. 2 shows this evolution of the spectral index. In the last column of the table, the unabsorbed flux in the energy range of 0.5-10 keV is given. This is the total flux for each region, the different sizes of the region is not reflected in these flux values.

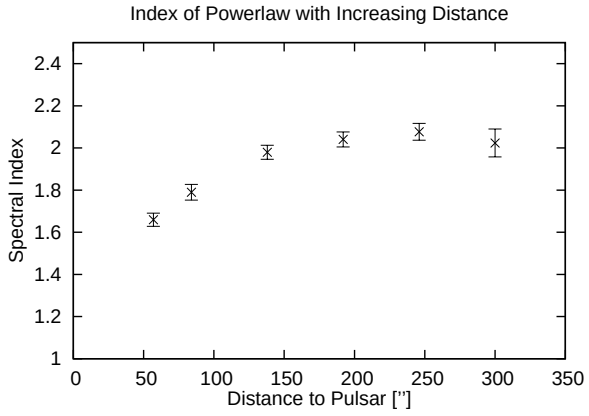

Fig. 2. Spectral index of the powerlaw fit to the XMM-Newton data of the different regions versus the mean distance of the extraction regions to the pulsar.

IV. The Model

At the pulsar wind shock, particles are accelerated and injected into the PWN. For our model, we assume a particle injection spectrum at the shock and propagate the particles radially outward. The shape of the spectrum is chosen on observational constraints rather than on a detailed physical model, which would be beyond the scope of our model. The particle injection spectrum $Q_0(E_e, t)$ at the shock radius R_S is assumed to be a single powerlaw with a spectral index of 2. This index corresponds to an observed synchrotron spectrum index of 1.5 at the shock radius. The minimum energy of the electrons is taken to be equal to the electron rest mass, $E_{e,min} = 8.2 \times 10^{-7}$ erg. The maximum energy of the electrons is constrained by two conditions as laid out in more detail in [14]. The first one is due to the fact that for charged particles confined within the shock radius, their Larmor radii R_L must be smaller than R_S. The parameter ϵ is defined as the ratio of these two radii, $\epsilon = R_L/R_S$, and should be smaller than 0.5. The maximum particle energy is thus limited to

$$E_{e,max} < \epsilon e \kappa \sqrt{\frac{\sigma \dot{E}}{c(1+\sigma)}}. \quad (1)$$

In this expression, κ is the compression ratio at the shock, σ the magnetization parameter and $\dot{E}$ the spin-down luminosity of the pulsar. The second condition comes into effect for strong magnetic fields. The maximum particle energy in this case is limited by the synchrotron emission it radiates. This limits the maximum energy to

$$E_{e,max} < 43.84 B^{-1/2} \,\text{erg}. \quad (2)$$

The normalization of the particle spectrum is then given by the condition that

$$\int_{E_{e,min}}^{E_{e,max}} Q_0(E_e, t) E_e dE_e = \eta \dot{E}. \quad (3)$$

The parameter η is the conversion efficiency of the spin-down luminosity to the energy of the particles.

For the propagation of the particles in the nebular flow we use the approximation of spherical symmetry and strictly radial outflow of the pulsar wind. Using this approximation, Kennel & Coroniti [15] showed that the product of the flow velocity v, the distance from the pulsar r and the magnetic field B is a constant:

$$Bvr = B_S v_S R_S = \text{const}, \quad (4)$$

where the subscripted parameters denote the parameters at the shock. The post-shocked magnetic field is given by ([15] and [16])

$$B_S = \frac{\Omega}{R_S} \sqrt{\frac{\dot{E}}{c}}. \quad (5)$$

In this equation and for the parameter optimization we use $\Omega = \kappa \sqrt{\sigma/(1+\sigma)}$ as a combined parameter for the shock compression and magnetization.

The velocity of the radial outflow is described with a profile of the form

$$v(r) = v_S \left(\frac{R_S}{r} \right)^{\alpha}. \quad (6)$$

By using this relation and Equation 4 we are able to write the magnetic field as a function of the distance to the pulsar and thus it is possible to calculate the flow parameters B and v for each point in the PWN. Following this relation, the age of the particle population is also known throughout the whole nebula.

The next step is to look at the evolution of the lepton spectrum as the particles move away from the pulsar wind shock. The particles lose energy due to adiabatic losses and synchrotron radiation in the PWN magnetic field. The total energy loss of the particles is given by (see [17]):

$$\frac{dE}{dt} = -\frac{E_e}{3} \nabla \cdot \mathbf{v}_\perp(r) - 2.368 \times 10^{-3} (B_\perp(r) E_e)^2. \quad (7)$$

Using expression 6, the adiabatic losses for the outflowing particles then are equal to

$$\frac{dE_{ad}}{dt} = \frac{v_S(2-\alpha)}{3R_S} \left(\frac{R_S}{r} \right)^{\alpha+1} E_e. \quad (8)$$

The transport equation is now numerically solved by spatially dividing the pulsar wind nebula into a number of shells. We start with the calculation of the lepton injection spectrum at the shock and then propagate this spectrum outwards, taking into account the energy losses for each shell/time step. The number of spatial shells and the binning of the spectra for each shell are chosen large enough to provide a convergent solution for the particle and emission spectra.

For each spatial shell we calculate the spectra of the emitted synchrotron and inverse Compton radiation due to the particle population contained in that shell. An outline of this procedure can be seen in Fig. 3. The model thus provides us with the lepton and emission spectra at each point within the PWN. We are then able to add up the shells from the model calculation to match the regions as observed in the XMM-Newton analysis (see Section III. The measured synchrotron spectra thus set constraints on the free model parameters. These are the shock parameters as stated in this section ($R_S, v_S, \epsilon, \alpha, \eta$ and Ω, the combined κ and σ parameter).

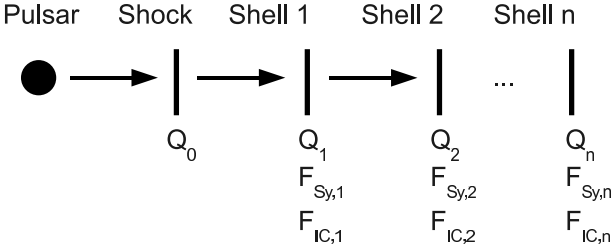

Fig. 3. Sketch of the model as described in this paper. Q denotes the lepton spectra with increasing distance, F_{Sy} and F_{IC} the emission due to the synchrotron and inverse Compton processes.

V. Parameter Optimization, Results and MSH 15−5*2* in TeV gamma-rays

Details on the optimization of the free model parameters and the results thereof will be presented at the conference. Based on the measured synchrotron emission of each of the ring regions used for the XMM-Newton analysis (as laid out in Section III), we will be able to constrain the shock parameters of MSH 15−5*2*. Using the obtained parameters, we will then be able to make predictions for the TeV emission of the central $0.1°$-region of the PWN. A comparison with the spatially resolved γ-ray emission as measured by the H.E.S.S. experiment will enable us to put an even stronger constraint on the shock parameters of this object.

VI. Conclusion

We analyzed XMM-Newton data of the SNR MSH 15−5*2* to derive the spatially resolved spectral parameters of the source. For the first time, such an analysis of the jet-region of MSH 15−5*2* was carried out. A steepening of the spectrum with increasing distance to the pulsar is observed. A numerical MHD model was developed to derive the shock parameters based on the X-ray analysis. We presented the model and will present the results of the of the parameter optimization process at the conference.

References

[1] B. Y. Mills, O. B. Slee, and E. R. Hill, *Australian Journal of Physics*, vol. 14, pp. 497–+, Dec. 1961.
[2] F. D. Seward and F. R. Harnden, Jr., *ApJL*, vol. 256, pp. L45–L47, May 1982.
[3] V. M. Kaspi et al., *ApJL*, vol. 422, pp. L83–L86, Feb. 1994.
[4] B. M. Gaensler et al., *MNRAS*, vol. 305, pp. 724–736, May 1999.
[5] E. Trussoni et al., *A&A*, vol. 306, pp. 581–+, Feb. 1996.
[6] K. Tamura et al., *PASJ*, vol. 48, pp. L33–L36, Jun. 1996.
[7] B. M. Gaensler et al., *ApJ*, vol. 569, pp. 878–893, Apr. 2002.
[8] T. Mineo et al., *A&A*, vol. 380, pp. 695–703, Dec. 2001.
[9] M. Forot et al., *ApJL*, vol. 651, pp. L45–L48, Nov. 2006.
[10] F. Aharonian et al., *A&A*, vol. 435, pp. L17–L20, May 2005.
[11] F. Jansen et al., *A&A*, vol. 365, pp. L1–L6, Jan. 2001.
[12] M. J. L. Turner et al., *A&A*, vol. 365, pp. L27–L35, Jan. 2001.
[13] L. Strüder et al., *A&A*, vol. 365, pp. L18–L26, Jan. 2001.
[14] O. C. de Jager and A. Djannati-Ataï, *ArXiv e-prints*, Mar. 2008.
[15] C. F. Kennel and F. V. Coroniti, *ApJ*, vol. 283, pp. 694–709, Aug. 1984.
[16] R. R. Sefako and O. C. de Jager, *ApJ*, vol. 593, pp. 1013–1023, Aug. 2003.
[17] O. C. de Jager and A. K. Harding, *ApJ*, vol. 396, pp. 161–172, Sep. 1992.